

Ca²⁺ pre-intercalated bilayered vanadium oxide for high-performance aqueous Mg-ion batteries

Qiang Fu^{a,*}, Xiaoyu Wu^b, Xianlin Luo^a, Ziming Ding^{c,g}, Sylvio Indris^a, Angelina Sarapulova^a, Zhen Meng^d, Morgane Desmau^e, Zhengqi Wang^a, Weibo Hua^{a,f}, Christian Kübel^{c,g,h}, Björn Schwarz^a, Michael Knapp^a, Helmut Ehrenberg^a, Yingjin Wei^{b,*}, Sonia Dsoke^a

^a Institute for Applied Materials (IAM), Karlsruhe Institute of Technology (KIT), Hermann-von-Helmholtz-Platz 1, D-76344 Eggenstein-Leopoldshafen, Germany

^b Key Laboratory of Physics and Technology for Advanced Batteries (Ministry of Education), College of Physics, Jilin University, 2699 Qianjin Street, Changchun 130012, PR China

^c Institute of Nanotechnology (INT), Karlsruhe Institute of Technology (KIT), Hermann-von-Helmholtz-Platz 1, D-76344 Eggenstein-Leopoldshafen, Germany

^d Helmholtz Institute Ulm for Electrochemical Energy Storage (HIU), Helmholtzstrasse 11, 89081 Ulm, Germany

^e Deutsches Elektronen-Synchrotron (DESY), Notkestr. 85, Hamburg 22607, Germany

^f School of Chemical Engineering and Technology, Xi'an Jiaotong University, No.28, West Xianning Road, Xi'an, Shaanxi 710049, PR China

^g Technische Universität Darmstadt, 64289 Darmstadt, Germany

^h Karlsruhe Nano Micro Facility (KNMF), Karlsruhe Institute of Technology (KIT), Eggenstein-Leopoldshafen 76344, Germany

ARTICLE INFO

Keywords:

Aqueous Mg-ion batteries
Vanadium oxide cathode
Aqueous Mg-ion electrolyte
In operando synchrotron diffraction
In operando X-ray absorption spectroscopy

ABSTRACT

The “oxygen-rich” Ca²⁺ pre-intercalated bilayered vanadium oxide (CaVOnH) was synthesized *via* hydrothermal method and determined as a monoclinic structure with reasonable lattice parameters. CaVOnH achieves a first discharge capacity of 273 mAh g⁻¹ with capacity retention of 91% at 50 mA g⁻¹ in 0.8 m Mg(TFSI)₂–85%PEG–15%H₂O (polyethylene glycol, PEG), but limited rate capability due to the low ionic conductivity of electrolyte. Dimethyl sulfoxide (DMSO) is used as a co-solvent to tune the physical-chemical properties of aqueous Mg-ion electrolyte (AME), resulting in the reorganization of Mg²⁺ solvation and hydrogen bond network. The AME containing DMSO shows improved ionic conductivity, low viscosity, and high Mg²⁺ diffusion coefficient and allows CaVOnH and V₂O₅ to achieve a much-improved rate capability and capacity. Moreover, the reaction mechanism and reversibility of CaVOnH are elucidated by combining *in operando* and *ex situ* techniques. The results demonstrate that CaVOnH undergoes 2-phase reaction and solid solution, the variation of oxidation state and the local environment of vanadium, and reversible formation/decomposition of MgF₂ cathode electrolyte interface during Mg²⁺ (de)intercalation, where MgF₂ originated from the decomposition of TFSI⁻.

1. Introduction

Rechargeable magnesium batteries (RMBs) have been considered as a promising candidate to replace Li-ion batteries (LIBs) in large-scale energy storage due to the notable advantages of Mg such as low cost, rich resources, high safety, and high volumetric capacity. Many efforts have been made to design and improve the performance of RMBs with nonaqueous electrolytes [1–3]. However, RMBs still face many challenges for commercialization because of the limited stability of the nonaqueous electrolytes, the lack of suitable cathode materials, the sluggish Mg-ion solid diffusion, and the irreversible Mg plating/stripping at the anode [4–7]. Besides, most nonaqueous Mg-ion electrolytes are

sensitive to moisture and should be prepared and handled in a strict atmosphere, which may cause safety concerns in practical applications [6,8]. As an alternative to the nonaqueous system, aqueous magnesium-ion batteries (AMIBs) are very attractive owing to the merits of aqueous electrolytes [1,9]. Moreover, the use of aqueous electrolytes makes battery manufacturing more convenient. To date, several cathode materials were evaluated in different aqueous Mg-ion electrolytes (AMEs), such as Prussian blue nickel hexacyanoferrate [10], Mg_xLiV₂(P O₄)₃ [9], and Mg-containing oxide cathodes (Mg_{1.1}Mn₆O₁₂·4.5H₂O [11], MgMn₂O₄/rGO [12], and MgFe_xMn_{2-x}O₄ [13]). For example, Chen et al. [10] reported an AMIB system based on a Prussian blue nickel hexacyanoferrate cathode, a polyimide anode, and a 1 M MgSO₄ electrolyte.

* Corresponding authors.

E-mail addresses: qiang.fu@kit.edu (Q. Fu), yjwei@jlu.edu.cn (Y. Wei).

<https://doi.org/10.1016/j.ensm.2024.103212>

Received 25 October 2023; Received in revised form 4 January 2024; Accepted 19 January 2024

Available online 28 January 2024

2405-8297/© 2024 The Author(s). Published by Elsevier B.V. This is an open access article under the CC BY license (<http://creativecommons.org/licenses/by/4.0/>).

Wang et al. [9] used a concentrated 4 m (“m” means “mol/kg”) magnesium bis(trifluoromethanesulfonyl)imide ($\text{Mg}(\text{TFSI})_2$) to expand the electrochemical stability window (ESW) of the electrolyte to 2.0 V, which enabled the use of $\text{Mg}_x\text{LiV}_2(\text{PO}_4)_3$ cathode and poly pyromellitic dianhydride (PPMDA) anode. Despite these progresses, the energy density of AMIBs is seriously limited by the low ESW (1.3–2 V) of AME [9,10,14] and AMIBs are still at their early stage because of the lack of high-performance cathodes.

Many efforts have been made to explore cathode materials over the past years. Several polymorphs of V_2O_5 framework have been studied as cathode materials for Li-, Na-, K-, and Mg- ion batteries[5,15–18]. In particular, the thermodynamically stable V_2O_5 (orthorhombic), having a layered structure comprising up-up-down-down-facing VO_5 square pyramids by sharing edges and corners, has been extensively investigated for various intercalated cations⁵. However, orthorhombic V_2O_5 delivers limited capacity and suffers from sluggish Mg^{2+} diffusion into the host. Whereas, bilayered vanadium oxide ($\text{V}_2\text{O}_5 \cdot n\text{H}_2\text{O}$) brings about new light to the battery research and can contribute an increased capacity since the present water notably extends the interplanar spacing from ~ 4.4 Å for V_2O_5 to ~ 11.5 Å for $\text{V}_2\text{O}_5 \cdot n\text{H}_2\text{O}$ and helps to shield the charge of Mg^{2+} cations during electrochemical processes. Meanwhile, pre-intercalated ions such as Mg^{2+} and Mn^{4+} are believed to form “pillars” with O atoms and improve the structural stability of $\text{V}_2\text{O}_5 \cdot n\text{H}_2\text{O}$ during Mg^{2+} (de)intercalation[19,20]. For example, Xu et al. [20] reported that $\text{Mg}_{0.3}\text{V}_2\text{O}_5 \cdot 1.1\text{H}_2\text{O}$ with Mg^{2+} and crystal water between layers delivered an initial discharge capacity of 164 mAh g^{-1} at 100 mA g^{-1} , with no capacity fading after 500 cycles. Despite their good cycling stability, these materials still show limited capacity.

Herein, new Ca^{2+} pre-intercalated hydrated vanadium oxide (CaVOnH) nanowires with large interplanar spacing were synthesized via hydrothermal method and used as cathode. The electrochemical performance of CaVOnH cathode is investigated in a newly developed electrolyte 0.8 m $\text{Mg}(\text{TFSI})_2$ -85%PEG-15% H_2O (polyethylene glycol, PEG)[21]. CaVOnH shows an initial discharge/charge capacity of 273/274 mAh g^{-1} with $\sim 100\%$ initial coulombic efficiency and 91% of capacity retention after 110 cycles, which is much higher than that of V_2O_5 in previous work (91% initial coulombic efficiency and yielding 80% of capacity retention)[21]. In addition, dimethyl sulfoxide (DMSO) is considered an ideal candidate solvent [22] and used as a co-solvent to improve the properties of AME (i.e., enhancing the ionic conductivity and decreasing the viscosity). A series of AMEs containing different amounts of DMSO were prepared: 0.8 m $\text{Mg}(\text{TFSI})_2$ -(85%-y) PEG-yDMSO-15% H_2O (y = 0, 10%, 20%, and 35%) and comprehensively studied by experiments and theoretical calculations. 20% DMSO-containing electrolyte was chosen as an optimized electrolyte, which allows CaVOnH and V_2O_5 to achieve a much improved capability and capacity. Furthermore, the reaction mechanism of CaVOnH was carefully studied using *operando* synchrotron diffraction and X-ray absorption spectroscopy (XAS) together with *ex situ* techniques such as X-ray powder diffraction (XRD), Raman scattering, and X-ray photoelectron spectroscopy (XPS).

2. Results and discussion

2.1. Structural and morphological characterizations of CaVOnH

To demonstrate the applicability of the electrolytes, CaVOnH nanowires synthesized via hydrothermal method were used as a cathode material for AMIBs. XRD was performed to study the structure of the synthesized vanadium oxide. The XRD cannot be indexed with any known structure in literature including $\delta\text{-Ca}_{0.25}\text{V}_2\text{O}_5 \cdot \text{H}_2\text{O}$, which is composed of δ -type V_2O_5 layers stacking along the *c* axis and with hydrated Ca^{2+} ions in between interlayers[23]. CaVOnH shows a similar XRD pattern as that of electrolytic vanadium oxide ($\text{e-V}_2\text{O}_5$)[24] and $\text{e-M}_x\text{V}_2\text{O}_5 \cdot y \cdot n\text{H}_2\text{O}$ [25], confirming the features of xerogel structure. It consists of double-layered VO_6 octahedra and VO_5 pyramids, while

water molecules and metal cations reside between the interlayers. CaVOnH has a strong reflection located at 2θ of $\sim 3.1^\circ$, corresponding to an interlayer spacing of ~ 13 Å (Fig. 1a). This value is much larger than those of $\text{V}_2\text{O}_5 \cdot 0.5\text{H}_2\text{O}$ (10.8 Å)[26], $\zeta\text{-V}_2\text{O}_5$ (~ 9.5 Å)[16], $\text{Zn}_{0.25}\text{V}_2\text{O}_5 \cdot n\text{H}_2\text{O}$ (~ 10.2 Å)[27], $\text{Mg}_{0.3}\text{V}_2\text{O}_5 \cdot 1.1\text{H}_2\text{O}$ (~ 11.9 Å)[20], $\text{NH}_4\text{V}_4\text{O}_{10} \cdot n\text{H}_2\text{O}$ (10.9 Å)[28], and $\text{NH}_4\text{V}_4\text{O}_{10}$ (9.8 Å)[29]. The large spacing distance of CaVOnH provides more space for Mg^{2+} and facilitates Mg^{2+} diffusion. Le Bail fitting based on the diffraction data indicates that the CaVOnH material could have a monoclinic structure with lattice parameters of $a = 5.0195$ Å, $b = 12.8764$ Å, $c = 3.6015$ Å, and $\beta = 94.694^\circ$. Scanning electron microscopy (SEM) demonstrates a nanowire morphology with typical lengths of 500 nm to 3 μm and width of ~ 50 nm (Fig. 1b). Selected area electron diffraction (SAED) and nano beam electron diffraction (NBED) were performed to further evaluate the lattice parameters and crystal structure in different orientations. To minimize the effect of the electron beam on the sample, these electron diffractions were acquired on the pristine CaVOnH nanowires (Fig. 1c and d) and carbon coated samples (Figs. 1e and S1) under low-dose conditions. Based on the structural prediction from the Le Bail fitting, these diffraction patterns can be indexed as $[-210]$, $[-201]$, and $[1-10]$ of zone axes. The *d*-spacing of crystal plane under different zone axes are listed in Table 1 & Fig. S1. It is found that the *d*-spacings acquired on both pristine and carbon coated sample are the same and fit well to the *d*-values obtained from XRD except for the (010) lattice spacing. The smaller *d*-value of (010) can presumably be attributed to a loss of crystal water between interlayers due to the high vacuum condition in the transmission electron microscope and under the electron beam. The other *d*-values are not significantly affected by this change of the (010) lattice parameters. This demonstrates that the lattice parameters proposed based on the XRD are reasonable for the new CaVOnH material.

Furthermore, thermogravimetric analysis (TGA), XPS, and inductively coupled plasma optical emission spectroscopy (ICP-OES) were performed to determine the amount of crystalline water and the ratio of Ca/V in the material. In the TGA curve (Fig. S2a), the weight loss of $\sim 12.5\%$ in the range of 100–400 °C is attributed to crystal water. ICP-OES reveals that the ratio of Ca/V in the nanowires is 0.219:2. The V 2p spectrum of the pristine CaVOnH can be fitted by two doublets with V 2p_{3/2} at 517.2 and 515.9 eV[30], respectively, resulting in an average oxidation state of $\text{V}^{4.92+}$ (inset of Figure S2a). To maintain charge neutrality, additional oxygen should exist in the material and, thus, the chemical formula of CaVOnH nanowires is determined as $\text{Ca}_{0.219}\text{V}_2\text{O}_{5+\delta} \cdot n\text{H}_2\text{O}$ ($\delta \sim 0.14$, $n \sim 1.51$). To prove the existence of additional oxygen, TGA coupled with mass spectrometry (TGA-MS) was done under Ar flow. Fig. S2b exhibits the observed *m/z*-signals of 16, 17, and 18 at ~ 200 °C, where *m/z* = 17 and 18 are due to water release and *m/z* = 16 is ascribed to O_2 release. Note that the observed *m/z*-signals of 44 at ~ 350 °C is due to CO_2 release that is assigned to the residual organic acetate component (CH_3COO^-) during synthesis.

Magnetic properties of CaVOnH were investigated to learn about the electronic configurations of V ions. Magnetic dc susceptibility vs. temperature mainly shows a Langevin-type paramagnetic signal stemming from localized paramagnetic centres ascribed to the V^{4+} ions that contribute with a single unpaired electron with a paramagnetic effective moment of $\mu_{\text{eff}} = 1.73 \mu_{\text{B}}$ each (V^{5+} is only diamagnetic and does not contribute to Langevin type magnetism). From the Curie-Weiss fit of CaVOnH, *C*, θ , and χ_{D} are estimated as 0.00731(6) $\text{cm}^3 \text{K mol}^{-1}$, -0.55 (2) K, and $-1.16(2) \cdot 10^{-4} \text{cm}^3 \text{mol}^{-1}$, respectively (Fig. 1f). Herein, the concentration of 1.9805(2) V^{5+} and 0.0195(2) V^{4+} per formula unit adding up to two V ions in total are determined, suggesting only a small portion of V^{4+} in CaVOnH. The corresponding saturation magnetization of 0.0194(2) μ_{B} (with 1 μ_{B} from each V^{4+}) is almost reached at 2 K and 7 Tesla in the field scans (Fig. S3a). To keep charge neutrality, the case of more oxygen according to $\delta_{\text{mag}} \sim 0.21$ in CaVOnH structure is in good agreement with the chemical analysis and TGA-MS results. Moreover, the susceptibility vs. temperature plot exhibits small ‘irregularities’ around 50 K (blue circle in Fig. 1f), suggesting a spin-glass-like

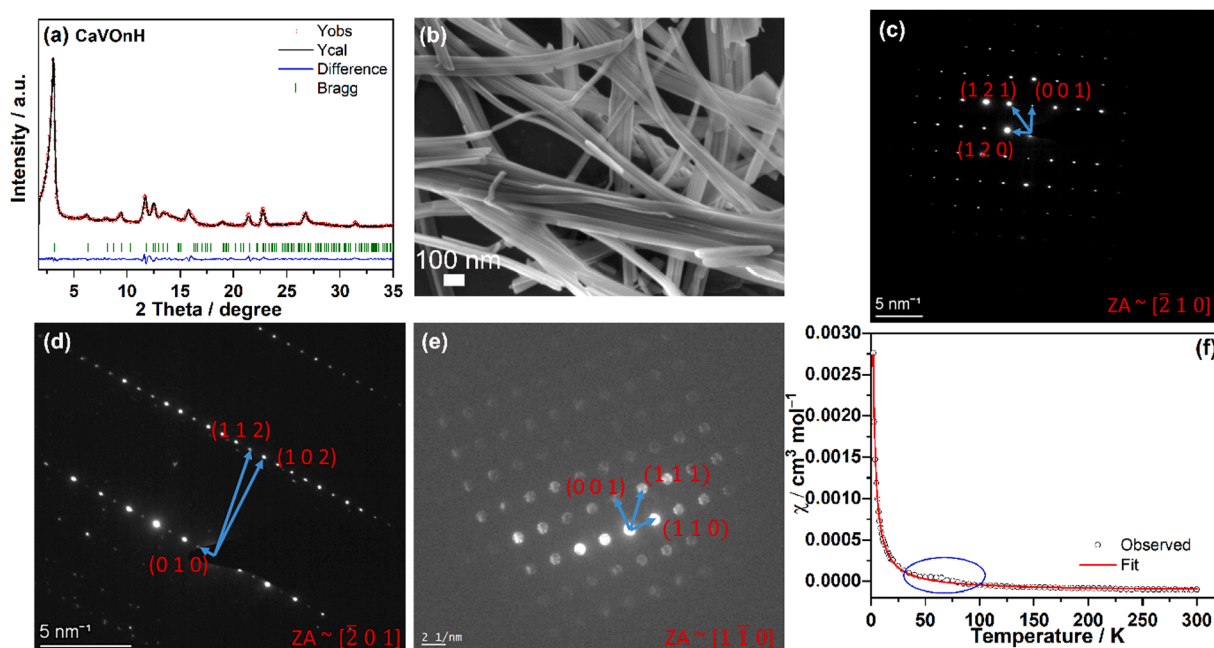


Fig. 1. Le Bail fitting based on X-ray diffraction data (Mo $K_{\alpha 1}$, $\lambda=0.70932$ Å) (a), SEM (b), selected area electron diffraction (SAED) (c, d) and nano beam electron diffraction (NBED) patterns (e) of CaVOnH nanowires in different orientations, and magnetic susceptibility χ vs temperature at 0.5 Tesla together with Curie-Weiss fit (f), where T , C , θ , and χ_D refer to temperature, Curie constant, Curie-Weiss temperature, and diamagnetic contribution, respectively.

Table 1

d-spacing obtained from XRD and SAED/NBED under different zone axes.

Crystal plane	(110)	(001)	(111)	(120)	(121)	(010)	(112)	(102)
d (nm) from TEM	0.46	0.36	0.28	0.40	0.27	1.15	0.16	0.17
d (nm) from XRD	0.47	0.36	0.27	0.40	0.26	1.29	0.16	0.17

behaviour, which is also revealed by the time-dependent evolution of magnetization at 50, 60, and 65 K (Fig. S3b).

2.2. Electrochemical properties of CaVOnH nanowires

The electrochemical properties of CaVOnH were first studied in 0.8 m $\text{Mg}(\text{TFSI})_2$ -85%PEG-15% H_2O using three-electrode cells. Fig. 2a shows the cyclic voltammetry (CV) of CaVOnH at 0.05 mV s^{-1} . The material displays three broad reduction peaks at around 2.6, 2.2, and 1.8 V and three broad oxidation peaks at 2.3, 2.73, and 3.14 V. In the following scans, both the reduction and oxidation peaks show only slight changes in intensity, indicating good electrochemical reversibility. With increasing the scan rate, the overall CVs of CaVOnH do not change much (Fig. 2b), but the redox peaks become wider and move toward lower/higher potentials for reduction/oxidation. Generally, peak current (i) and scan rate (v) obey the power-law relationship[31] of $i = av^b$. According to the linear fitting of $\log(i)$ vs. $\log(v)$, the oxidation/reduction of CaVOnH exhibits b values of 0.6/0.71 (Fig. 2c), indicating a diffusion-controlled process.

Charge-discharge cycling of the CaVOnH nanowires was performed in the voltage window of 1.58–3.68 V. The material displays slope-like discharge/charge profiles at 50 mA g^{-1} and delivers a first discharge/charge capacity of 273/274 mAh g^{-1} , resulting in $\sim 100\%$ initial coulombic efficiency (CE, Fig. 2d). During subsequent cycling, CaVOnH provides a discharge capacity of 249 mAh g^{-1} with 91% capacity retention after 110 cycles (Fig. 2e). As shown in Fig. 2 g, CaVOnH delivers a capacity of 253, 206, 157, 87, and 41 mAh g^{-1} at 50, 100, 200, 500, and 1000 mA g^{-1} , respectively. After returning to 50 mA g^{-1} , the discharge capacity recovers to 253 mAh g^{-1} with negligible capacity decay after 45 cycles. The electrode exhibited larger and larger electrode

polarization with the increase of specific current (Fig. 2f). Compared with V_2O_5 in previous work[21], the voltage profiles of CaVOnH are somewhat different, where V_2O_5 displays more distinct plateau features, indicating different structural changes during Mg^{2+} intercalation. V_2O_5 nanowires show a much higher first discharge capacity of 359 mAh g^{-1} with low CE of 91%. But, the discharge capacity decreases to 286 mAh g^{-1} after 100 cycles with 80% of capacity retention[21]. Obviously, CaVOnH exhibits better cycle stability than that of V_2O_5 . However, CaVOnH, which has a larger interlayer spacing of ~ 13 Å than that of V_2O_5 (4.4 Å), does not exhibit a much higher capacity than that of V_2O_5 at current density > 500 mA g^{-1} , indicating that the kinetics properties of CaVOnH at high current densities strongly rely on the ionic conductivity (and viscosity) of electrolyte.

2.3. Study of DMSO-containing AMEs

To further improve the electrolyte properties (i.e., higher ionic conductivity and lower viscosity), an organic solvent with low viscosity and easily dissolved with PEG and water is strongly recommended. Meanwhile, many other factors, such as low toxicity, high boiling point, thermal stability, and high electrochemical stability, should be considered as well. Herein, DMSO is considered an ideal candidate solvent[22] and used as a co-solvent to improve the properties of AME. A series of AMEs containing different amounts of DMSO were prepared: 0.8 m $\text{Mg}(\text{TFSI})_2$ -(85%- y)PEG- y DMSO-15% H_2O ($y = 0, 10\%, 20\%$, and 35%). Along with the increase of DMSO, the ionic conductivity of the AMEs notably increases (Fig. 3a) and the viscosity strongly decreases (Fig. 3b), which matches well with Walden's rule[32] (Fig. 3c). The ionic conductivity of the electrolyte with 20%DMSO is three times higher than that of the DMSO-free one. Moreover, the ESW of the electrolytes was

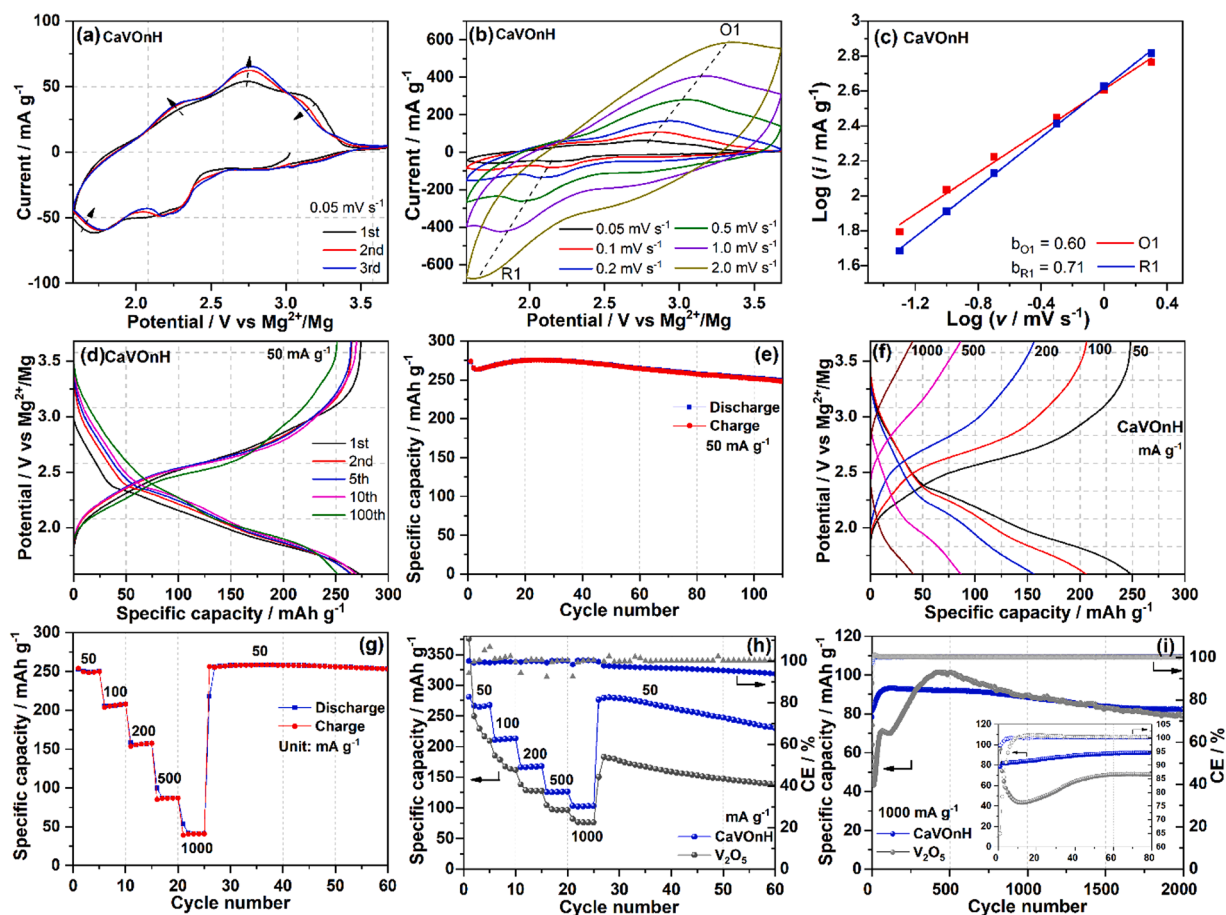


Fig. 2. Cyclic voltammetry (CV) of CaVOH in 0.8 m Mg(TFSI)₂-85 %PEG-15 %H₂O at a scan rate of 0.05 mV s⁻¹ (a), where the arrows indicate the tendency of changes from the first to the third cycle, CV curves at different sweeping rates (b) and their log(*i*) vs log(*v*) plots and linear fittings (c), charge–discharge curves of CaVOH in 0.8 m Mg(TFSI)₂-85 %PEG-15 %H₂O at 50 mA g⁻¹ (d), cycling performance at 50 mA g⁻¹ (e), charge–discharge curves from rate performance (f), and rate performance (g); Rate performance (h) and cycling performance at 1000 mA g⁻¹ (i) of CaVOH and V₂O₅ in 0.8 m Mg(TFSI)₂-65 %PEG-20 %DMSO-15 %H₂O. All electrochemical properties were studied using three-electrode cells using CaVOH nanowires working electrode, activated carbon counter electrode, and AgCl/Ag reference electrode.

determined by linear sweep voltammetry (Fig. S4). Overall, only a minor change in ESW (0.48–4.08 V vs Mg²⁺/Mg) is obtained for 0.8 m Mg(TFSI)₂-65%PEG-20%DMSO-15%H₂O, compared with 0.8 m Mg(TFSI)₂-85%PEG-15%H₂O. The solvent structure of the electrolyte was studied by ¹H nuclear magnetic resonance (NMR) spectroscopy (Fig. S5). Along with the increase of DMSO, the ¹H peaks of H₂O and PEG shift to lower values of 4.85 and 3.72 ppm, respectively, indicating the increase of electron density around H and the lengthening of H–O bond in H₂O and C–H bond of PEG. While the ¹H peak of DMSO slightly shifts to higher values with increase in intensity, confirming the local structural changes of H by adding DMSO. Consequently, 0.8 m Mg(TFSI)₂-65%PEG-20%DMSO-15%H₂O is selected as the optimal electrolyte due to its high ionic conductivity, acceptable viscosity, wide ESW, and high safety (Fig. S6, Video S1–2).

Theoretical analysis was performed to study the solvent properties of the series AMEs. First, the hydrogen bonds (HBs) of the electrolytes were calculated by molecular dynamics (MD) simulations. The HBs of 0.8 m Mg(TFSI)₂-85%PEG-15%H₂O are contributed by TFSI⁻-H₂O interaction (~5.4 per TFSI⁻), H₂O–H₂O interaction (~1.5 per H₂O), and PEG–H₂O interaction (~1.9 per PEG)[21]. For the electrolyte containing 20% DMSO, an additional interaction of DMSO–H₂O (~0.5 per DMSO) is observed with a slight decrease of PEG–H₂O contribution (~1.7 per PEG), while the contributions from TFSI⁻-H₂O and H₂O–H₂O remain unchanged. Therefore, the changes of HBs affect the ¹H chemical shift of the electrolytes, which is consistent with the NMR results. Besides, the

lifetime of HBs slightly increases to 82 ps from 79 ps, demonstrating higher stability of the electrolyte containing 20%DMSO than that of 0.8 m Mg(TFSI)₂-85%PEG-15%H₂O.

Molecular dynamics (MD) (Fig. 3d–i, Tables S1 and S2) demonstrate that the AME containing 20%DMSO reaches a stable equilibrium state. The *g*(*r*) profiles of 0.8 m Mg(TFSI)₂-65%PEG-20%DMSO-15%H₂O show that the first solvation shell of Mg²⁺ consists of Mg²⁺-H₂O (0.19 nm), Mg²⁺-TFSI⁻ (0.22 nm), Mg²⁺-PEG (0.19 nm), and Mg²⁺-DMSO (0.21 nm) peaks. After adding DMSO, an additional peak at 0.21 nm is present compared with the DMSO-free one[21] in the previous work, corresponding to Mg²⁺-DMSO with an ICN=1.0. Meanwhile, the ICN of Mg²⁺-H₂O, Mg²⁺-TFSI⁻, and Mg²⁺-PEG decreases to 3.0, 0.4, and 1.4, respectively (Fig. 3 g and h). This indicates that some of the H₂O, PEG, and TFSI⁻ molecules in the first solvation shell are replaced by DMSO and thus tuning the physical-chemistry properties of the electrolytes. The transport property of Mg²⁺ in the electrolytes was further analyzed by calculating the mean square displacement. At room temperature, Mg²⁺ shows better diffusive behavior in the 0.8 m Mg(TFSI)₂-65%PEG-20%DMSO-15%H₂O compared with the electrolyte without DMSO (Fig. 3i). This is consistent with our hypothesis that the cation diffusivity is influenced by the viscosity of the electrolyte. Therefore, the introduction of DMSO can confer a better diffusion coefficient of Mg²⁺ than the DMSO-free 0.8 m Mg(TFSI)₂-85%PEG-15%H₂O electrolyte.

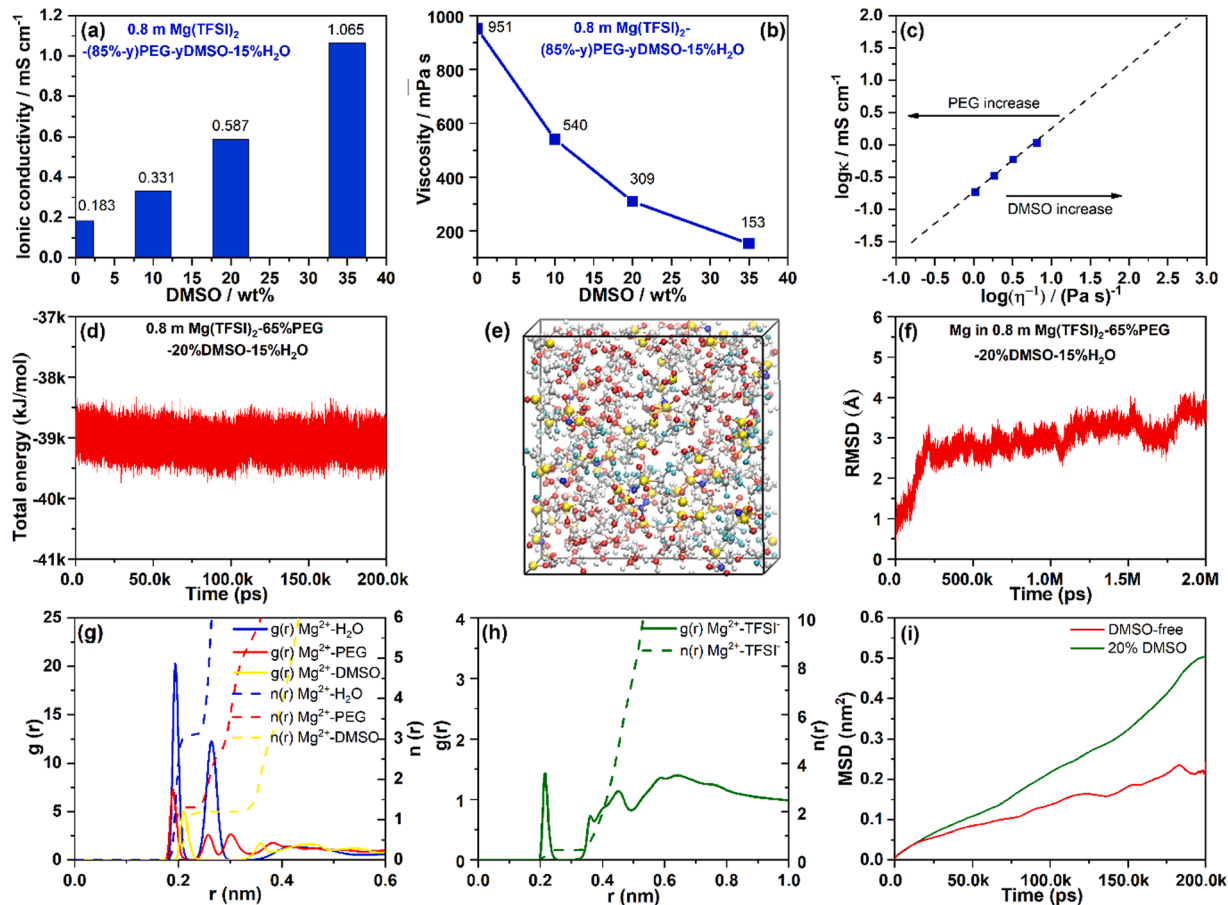


Fig. 3. Ionic conductivity (a) and viscosity (b) of a series of DMSO containing AMEs, 0.8 m Mg(TFSI)₂-(85-y)PEG-yDMSO-15%H₂O (y = 0, 10%, 20%, and 35%) and their log(η^{-1}) vs log(κ) plot (c), where all measurements were carried out at 25 °C, respectively; Molecular dynamics (MD) of electrolyte: Illustration of the evolution of the total energy (d), the simulated geometrical structure (e), root-mean-square deviation (RMSD) of Mg (f), and RDF g(r) and ICN n(r) of Mg²⁺-H₂O, Mg²⁺-PEG, Mg²⁺-DMSO (g) and Mg²⁺-TFSI⁻ (h) in the 0.8 m Mg(TFSI)₂-65%PEG-20%DMSO-15%H₂O system during MD simulation at 300 K, where hydrogen, carbon, oxygen, fluorine, magnesium, sulfur and nitrogen atoms are marked with white, gray, red, cyan, pink, yellow and blue, respectively; The mean square displacement (MSD) of Mg ions (i) in both DMSO-free and 20%DMSO electrolytes.

2.4. Electrochemical properties of CaVOnH and V₂O₅ in 20%DMSO-containing electrolyte

The rate capability and long cycling of CaVOnH and V₂O₅ were performed in the 20%DMSO-containing electrolyte (Fig. 2h and i). In 0.8 m Mg(TFSI)₂-65%PEG-20%DMSO-15%H₂O, both materials demonstrate much-improved rate capability at all specific currents compared to 0.8 m Mg(TFSI)₂-85%PEG-15%H₂O (Table S3), in particular at 1 A g⁻¹. CaVOnH shows a much better performance at all current densities in the improved electrolyte compared to V₂O₅ (Fig. 2h). Particularly, CaVOnH delivers an initial discharge capacity of 281 mAh g⁻¹, and capacity of 264, 212, 167, 126, and 102 mAh g⁻¹ at 50, 100, 200, 500, and 1000 mA g⁻¹, respectively. The discharge capacity can still recover to 279 mAh g⁻¹ when the current density returns to 50 mA g⁻¹. Unfortunately, in the 20%DMSO-containing electrolyte, the cycling stability of CaVOnH at low current density of 50 mA g⁻¹ is decreased a lot compared with DMSO-free one and this decrease could probably be attributed to the electrolyte decomposition at 50 mA g⁻¹. Further work needs to be done to understand the reason for poor cycling stability at low current density of 50 mA g⁻¹. Moreover, CaVOnH and V₂O₅ (Fig. 2i) deliver an initial discharge capacity of 78 and 96 mAh g⁻¹ at 1 A g⁻¹, respectively. CaVOnH reaches its highest capacity of 93 mAh g⁻¹ after activation due to the high current density applied (100 cycles), V₂O₅ reaches its highest capacity of 101 mAh g⁻¹ after activation (400 cycles), suggesting that the crystal water can shield the charge in the host structure. CaVOnH and V₂O₅ deliver discharge capacities of 82 and 79

mAh g⁻¹ after 2000 cycles, yielding capacity retention 88% and 78%, respectively. V₂O₅ experiences a large capacity fluctuation in the range of 43–101 mAh g⁻¹ at 1 A g⁻¹. As a result, CaVOnH and V₂O₅ overlap with each other at the 285th cycle and 1438th cycle under high current density of 1 A g⁻¹ and CaVOnH exhibits much higher capacity and better cycling stability in the next 500 cycles. This could be attributed to the different crystal structures of both CaVOnH and V₂O₅ materials. Overall, the addition of DMSO in Mg(TFSI)₂-PEG notably improves the electrochemical performance of vanadium oxides at both low and high current densities due to the higher ion conductivity, lower viscosity, and better diffusion coefficient of Mg²⁺ in the electrolytes. This result demonstrates that not only the ionic conductivity of the electrolyte but also the interplanar spacing and crystal water in the structure play an important role in improving electrochemical performance.

2.5. Reaction mechanism of CaVOnH in AMIBs

To reveal the structural evolution of CaVOnH upon Mg²⁺ intercalation, *in operando* synchrotron diffraction was performed during the initial discharge as shown in Fig. 4a. Before discharge, all reflections can be indexed on pristine CaVOnH except those reflections from Kapton foil and PTFE (Fig. S7). Upon 1st discharge (Region I), the reflection at 0.86° shifts to a higher angle with decrease in intensity, the rest of reflections of CaVOnH shift towards lower angles such as 3.39°, 3.45°, 5.11°, 6.21°, 6.61°, 6.77°, and 7.74°. Meanwhile, two reflections at 1.4° and 6.53° appear and gradually increase in intensity, demonstrating the 2-phase

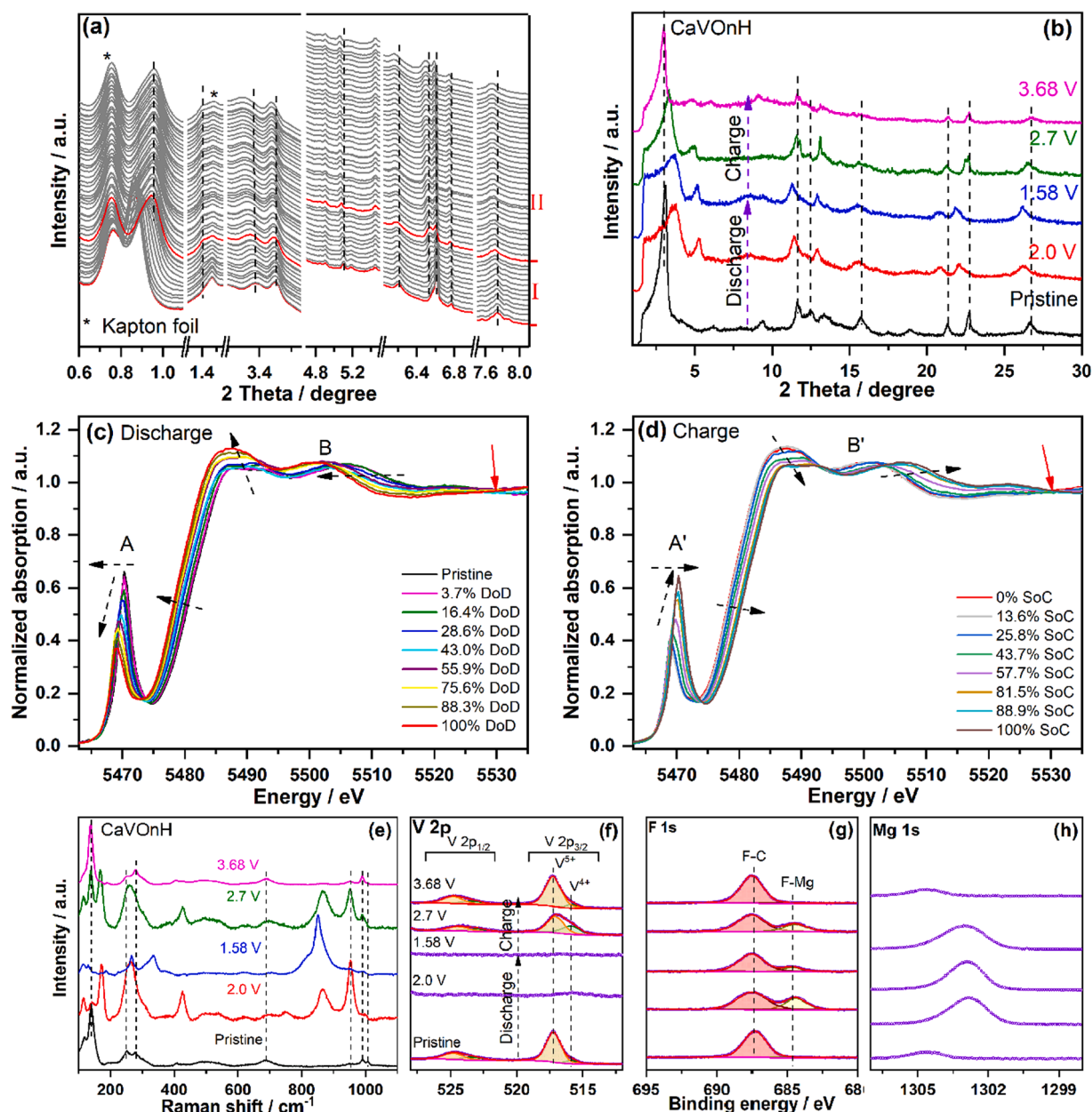


Fig. 4. *In operando* synchrotron diffraction of CaVOnH ($\lambda=0.20733$ Å, 60 keV) during the first discharge at a current density of 20 mA g⁻¹ (a) and *Ex situ* XRD (b) of CaVOnH at different discharge/charge states (Mo K_{α1} radiation, $\lambda=0.70932$ Å); *In operando* V K-edge XANES spectra of CaVOnH during the 1st cycle, where DoD and SoC refer to depth of discharge (c) and state of charge (d), respectively; the isosbestic points are pointed out by red arrows; *Ex situ* Raman spectra (e), and V 2p, F 1s and Mg 1s XPS spectra (f, g, h) of CaVOnH at different discharge/charge states (pristine, 2.0 V (about 50% of DoD), 1.58 V (about 100% of DoD), 2.7 V (about 50% of SoC), and 3.68 V (about 100% of SoC)).

reaction in Region I. With further Mg²⁺ intercalation, the reflections only show shifts to lower angles, indicating a solid solution process in Region II. Although the discharge profile does not show the same shape as the normal 3-electrode measurement, the structure changes can be properly explained since they are related to the amount of Mg²⁺ intercalation. *Ex situ* XRD was performed on the CaVOnH cathode at different states to further study/prove the structural evolution during Mg²⁺ intercalation/deintercalation (Fig. 4b). During Mg²⁺ intercalation, most reflections of CaVOnH gradually shift to lower angles while the one at 3.1° shifts to a higher angle with strong decrease in intensity and one new reflection at 5.28° is observed, indicating a 2-phase transition and the shrinking of interlayer spacing, in good agreement with *in operando* synchrotron diffraction. With full Mg²⁺ intercalation, all reflections slowly shift to lower angles, demonstrating a solid solution process.

Upon charging, all reflections recover to their initial positions with lower intensities, implying a reversible 2-phase transition but an asymmetry during cycling.

In operando XAS was carried out to reveal the variation of the oxidation state in CaVOnH and the local electron environment of V during cycling. Fig. 4c and d present the normalized V K-edge spectra during the first discharge-charge processes. The oxidation state of V in CaVOnH is determined as +4.85 using linear combination fitting (LCF) (Fig. S8a), which is in good agreement with the XPS result (Fig. 4f). Moreover, an intense pre-edge peak for the V K-edge is observed because of the five-fold coordinated V-ions by oxygens in a distorted tetragonal pyramid, which is ascribed to the transitions between the 1s and bound p-hybridized d-states[33,34]. CaVOnH shows a similar XAS feature as that of xero-gel material, implying a similar structure between CaVOnH

and e- V_2O_5 [24], which is also close to that of V_2O_5 . Upon Mg^{2+} intercalation, the edge position of the V K-edge slowly shifts to lower binding energies, suggesting the reduction of the V oxidation state (Fig. 4c). Meanwhile, the pre-peak (A in Fig. 4c) gradually shifts towards lower binding energy with a simultaneous decrease of intensity, indicating the reduction of V ions and the symmetry increase of local V environments. Since the increase in symmetry would decrease the probability of the 1s-3d transition, thus resulting in a decrease of the peak intensity[35]. The edge resonance (B in Fig. 4c) that is ascribed to the absorption of photons accompanied by core-electron excitations[34,36] exhibits distinct changes in both shape and intensity. During Mg^{2+} intercalation, two broad peaks centered at 5488 eV and 5493 eV converge into one broad peak centered at ~ 5487 eV with a gradual increase of intensity, while the peak at 5507 eV notably shifts to lower energy of 5501 eV with slight increase in intensity. Two distinct isosbestic points[37] at ~ 5530 eV (red arrows in Fig. 4c and d) are observed during both discharge and charge, demonstrating a 2-phase reaction[37] upon Mg^{2+} intercalation/deintercalation, as already proved by *in operando* synchrotron diffraction. At the fully discharged state, the V oxidation state of CaV-OnH is estimated to be +3.82 using LCF (Fig. S8b), which is very close to the value calculated from the electrochemical capacity (+3.85). Upon Mg^{2+} deintercalation, the edge energy of V K-edge, pre-edge peak, and edge resonance display reversible behaviors and return to their initial positions, indicating the oxidation of V ions and reversibility of local structure (Fig. 4d). The slight difference in the XAS before and after cycling might be explained by extraction of a small amount of Ca^{2+} from the structure (Fig. S9a and b). *Ex situ* XAS was carried out to look into the local structure changes of V ions by analyzing the phase-uncorrected Fourier transform (FT) (k^3 -weighted) of the V K-edge extended X-ray absorption fine structure (EXAFS). The pristine CaVOnH shows two FT peaks at 1.03 Å and 1.64 Å, corresponding to the V-O bonds in VO_6 octahedra, and one FT peak at 2.71 Å assigned to the V-V shell[38–40]. During discharge, the V-O features shift to lower radial distances with strongly increased (peak at 1.64 Å) and slightly decreased amplitudes (peak at 1.03 Å) (Fig. S9c), indicating the overall symmetry increase of the local structure around V. Meanwhile, the V-V feature decreases its amplitude with shifts to a lower value. These results indicate that the intercalated Mg^{2+} ions affect both the V-O and V-V shell structure. During charging, they show reversible behavior and almost return to their initial positions (Fig. S9d), demonstrating the high reversibility of CaVOnH.

The local structure changes of CaVOnH during Mg^{2+} (de)intercalation were further investigated by Raman scattering on the pristine and cycled samples (Fig. 4e). CaVOnH nanowires have the typical Raman peaks of V_2O_5 as reported in previous work[41]. Moreover, several additional Raman peaks are observed for CaVOnH (862, 954, and 1009 cm^{-1}), implying local structure changes due to Ca^{2+} pre-intercalation. Significant structural changes are detected for CaVOnH after half Mg^{2+} intercalation. Upon Mg^{2+} intercalation to 2.0 V, the peak at 140 cm^{-1} disappears and meanwhile, some new peaks appear at 173, 264, 427, 750, 867, and 955 cm^{-1} . With full Mg^{2+} intercalation to 1.58 V, only some broad peaks (266, 335, and 852 cm^{-1}) are seen due to the disordered local structure in the Mg_xCaVOnH phase. Upon charging, the Raman spectra show reversible changes and finally return to the original state of pristine CaVOnH, indicating that the changes driven by Mg^{2+} intercalation are highly reversible.

XPS is a powerful surface-sensitive technique and useful to investigate the surface chemistry and elemental composition of materials. XPS not only can display what elements are present but also to what other elements they are bonded to and, therefore, was performed on the pristine and cycled cathodes. The V 2p spectrum of pristine CaVOnH can be fitted by two doublets with V $2p_{3/2}$ at 517.2 and 515.9 eV[30], respectively, resulting in an average oxidation state of $\text{V}^{4.92+}$ (Fig. 4f–h). The V $2p_{3/2}$ peak is invisible after discharge and reappears after charge with $\text{V}^{4.64+}$ and $\text{V}^{4.92+}$, respectively. The F 1 s spectrum of pristine CaVOnH shows one peak at 687.3 eV related to C-F bond. Surprisingly,

two new peaks at 684.7 and 1303 eV appear upon discharging and then disappear upon charging for F 1 s and Mg 1 s, revealing the reversible formation and decomposition of MgF_2 related to the decomposition of TFSI^- . MgF_2 is identified as a dominant component of cathode electrolyte interphase (CEI) and the new peak at 1303 eV may be also correlated to other Mg-containing compounds contributing to CEI. Such a CEI consisting of main component of MgF_2 is also seen in the case of V_2O_5 based AMIBs[21], where the V $2p_{3/2}$ peak is still visible for V_2O_5 at the 50% of DoD. While, the invisible V $2p_{3/2}$ peak for CaVOnH at 50% of DoD suggests that the amount of CEI depends on the species of cathode material. Interestingly, $\text{Mg}_x(\text{OH})_y(\text{CH}_3\text{COO})_z$ CEI[42] was recently reported on the surface of discharged $\text{VO}_2(\text{B})$ cathode electrode in aqueous $\text{Mg}(\text{CH}_3\text{COO})_2$ solution. Solid electrolyte interphase containing MgF_2 on Mg anode[43] and MgF_2 -coated Mg anode[44] were also reported in organic electrolyte based Mg-ion batteries. Overall, the CaVOnH cathode returns to its pristine state, accompanied by reversible CEI formation and decomposition during cycling.

3. Conclusion

The existence of “excess oxygen” in CaVOH is proven by mass spectrometry and magnetic measurements to reach charge neutrality. CaVOnH exhibits high initial CE of $\sim 100\%$ and capacity retention of 91% at 50 mA g^{-1} in the 0.8 m $\text{Mg}(\text{TFSI})_2$ -85%PEG-15% H_2O , which is much higher than that of V_2O_5 (91% initial CE and capacity retention of 80%). The addition of DMSO tunes the electrochemical and physical-chemical properties of AME by changing the Mg-ion solvation and HBs network of AMEs and, therefore, improves the ionic conductivity, viscosity, and Mg^{2+} diffusion coefficient of AMEs. 0.8 m $\text{Mg}(\text{TFSI})_2$ -65%PEG-20%DMSO-15% H_2O was chosen as an optimal electrolyte with a stable ESW of ~ 3.6 V. Both CaVOnH and V_2O_5 demonstrate high rate capability and high capacity at high specific current in the DMSO-containing AME. The electrolyte can significantly affect the electrochemical performance of layered oxide electrode materials, particularly at high current densities. Moreover, the reaction mechanism and reversibility of CaVOnH during cycling were investigated via *in operando* and *ex situ* techniques. CaVOnH undergoes a 2-phase reaction and solid solution during discharge and charge processes. *In operando* XAS and *ex situ* EXAFS reveal the variation of the oxidation state and the local electron environment of V during Mg^{2+} intercalation/deintercalation together with Raman and XPS. Meanwhile, the reversible formation/decomposition of CEI in AMIBs is revealed, where MgF_2 originating from the decomposition of TFSI^- is identified as the dominant component. This work develops a new oxygen-rich layered vanadium oxide with large interlayer spacing, provides an approach to adjust the electrolyte solvation for multivalent ion batteries and helps understand the Mg^{2+} storage mechanism of cathode materials.

3.1. Experimental and calculations details

3.1.1. Synthesis of $\text{Ca}_x\text{V}_2\text{O}_{5+\delta}\cdot n\text{H}_2\text{O}$ nanowires

$\text{Ca}_x\text{V}_2\text{O}_{5+\delta}\cdot n\text{H}_2\text{O}$ (CaVOnH) nanowires were prepared via a hydrothermal method. Briefly, 0.5 g of commercial V_2O_5 powder (Alfa Aesar, 99.99%) was added to 20 ml of deionized water under vigorous stirring for 10 mins to form a light orange suspension. Then, 5 ml 30% hydrogen peroxide (H_2O_2) was dropwise added to the above suspension with stirring for 20 mins to get a transparent reddish-brown solution. Afterwards, a solution consisting of 0.1087 g of $\text{Ca}(\text{CH}_3\text{COO})_2$ dissolved in 5 ml deionized water was added into the above reddish-brown solution with stirring for 10 mins. The obtained solution was transferred to a 50 ml Teflon-lined stainless-steel autoclave and kept at 200 °C for 48 h. The precipitate was washed with deionized H_2O and ethanol several times and dried at 75 °C for 12 h.

3.1.2. Preparation and characterizations of the electrolyte

$\text{Mg}(\text{TFSI})_2$ was dissolved into a series of polyethylene glycol 400

(PEG-400), H₂O, and DMSO solvent with vigorous stirring overnight at room temperature to form 0.8 m Mg(TFSI)₂-(85%-y)PEG-yDMSO-15% H₂O (y = 0, 10%, 20%, and 35%). Ionic conductivity was measured by using Mettler Toledo InLab® 738 ISM at 25 °C. The viscosity of the electrolytes was measured on a Bohlin Gemini 200 Nano rheometer at 25 °C with 40/1° cone geometry by using a solvent evaporation protection cover. Measurements were conducted with the shear rate varied from 1 to 200 s⁻¹ (viscosity is generally independent of shear rate). ¹H nuclear magnetic resonance (NMR) spectroscopy was performed on the electrolyte samples with a Bruker Avance 300 MHz spectrometer at a magnetic field of 7.0 T. Samples were placed inside 5 mm glass tubes and chemical shifts are given relative to that of tetramethylsilane at 0 ppm.

3.1.3. Morphological and structural study

The morphologies were studied with a Zeiss Supra 55 Scanning Electron Microscope (SEM) with primary energy of 15 keV. The structural characterization was performed on a STOE STADI P diffractometer operated with Mo K_{α1} radiation (λ=0.70932 Å). The powders were filled in 0.5 mm Ø boro-silicate capillaries, and diffraction patterns were collected in capillary geometry. Thermogravimetric analyses (TGA) were done on STA 449C (Netzsch GmbH) under Ar flow to determine the crystal water content in CaVOnH. A LabRam HR Evolution Raman microscope from Horiba Scientific equipped with He-Ne laser (633 nm, 17 mW) and a CCD detector (Horiba) was used to collect the Raman scattering of the samples. Meanwhile, a 600 gr/mm grating was used to split the measurement signal with α×100 objective (NA 0.95) for all the pristine and cycled samples. SAED patterns were acquired using a ThermoFisher Themis 300 TEM with a dose rate of 76 e nm⁻² s⁻¹ at 300 kV. NBED patterns were acquired with 0.6 mrad convergence angle of electron beam and a nominal screen current of around 20 pA. In addition to characterization on the pristine CaVOnH nanowire, electron diffraction was also conducted on the carbon coated sample to minimize the electron beam damage. The analysis software of Jems[45] was used to help index the crystal structure. Magnetic properties were measured using the Vibrating Sample Magnetometry (VSM) option installed onto a DynaCool Physical Property Measurement System (PPMS) from Quantum Design. 10.5 mg of sample was filled into a polypropylene capsule for all measurements.

Dc magnetic moment was measured as a zero field cooled procedure from 2 K to 300 K at a field of 5000 Oe (0.5 T) in settle mode (from 2 K to 20 with 1 K temperature resolution and from 25 K to 300 K with 5 K temperature resolution). Magnetic moment vs field was measured at 2, 25, 60 and 100 K. Sample was cooled down to 2 K in zero field then magnetic moment was measured with a full loop starting from 7 T. Afterwards the sample was heated to the next temperature at 7 Tesla and another full loop was measured etc. Magnetization vs. time was done by setting the sample to 150 K and zero magnetic field. Then the sample was cooled down to the T_{iso} = 10, 20, 30, 40, 45, 50, 60, 65, 70, 80, 90 and 100 K, respectively, and the magnetization was measured for 30 min after a field of 1000 Oe was set with 200 Oe/sec.

Simultaneous thermogravimetric analysis and mass spectrometry (TGA-MS) were conducted with a Setaram thermal analyzer SENSYS evo TGA equipped with a Pfeiffer OmniStar mass spectrometer for the analysis of the evolved gas. The measurement was conducted from room temperature to 650 °C with a heating rate of 5 °C min⁻¹ under argon flow.

X-ray photoelectron spectroscopy (XPS) was performed using a K-Alpha spectrometer (ThermoFisher Scientific, UK) equipped with a microfocused, monochromated Al K_α X-ray source (λ=1486.6 eV) with a spot size of 400 μm. A charge compensation system was employed during measurement, using electrons of 8 eV energy and low-energy Ar ions to prevent localized charge accumulation. All samples were prepared in an Ar-filled glove box and transferred under an inert atmosphere into the spectrometer. Thermo Avantage software was used in data acquisition and processing, as described elsewhere[46]. The analyzer transmission function, Scofield sensitivity factors, and effective

attenuation lengths for photoelectrons were applied for quantification [47]. The standard TPP-2 M formalism was used for the calculation of effective attenuation lengths[48]. All spectra were referenced to the carbonaceous C 1 s peak (C-C/C-H) at 285.0 eV binding energy.

3.1.4. Electrochemical characterizations

The electrode was prepared by coating slurry mixture on a stainless steel foil, which consists of CaVOnH active material with C65 (Timcal) and polyvinylidene difluoride (PVDF) binder in a ratio of 70:20:10 with N-Methyl-2-pyrrolidone solvent. The electrode (mass loading of ~1.3 mg cm⁻²) was dried at 65 °C overnight and then cut into discs of 12 mm diameter. Activated carbon (AC) electrode was prepared using AC, C65 (Timcal), and polytetrafluoroethylene (PTFE, 60 wt% solution in water from Sigma-Aldrich) in a ratio of 8:1:1 with solvent isopropanol in a DAC150.1 FVZ model from SpeedMixer with 800 rpm for 10 min. The paste mixture was kneaded manually on a glass plate and finally was rolled to a uniform thickness electrode. The electrodes were finally dried at 70 °C overnight under vacuum before use.

The LSV of various electrolytes was performed using a glass cell consisting of glassy carbon (GC) working electrode, Pt plate counter electrode, and AgCl/Ag reference electrode. Three-electrode Swagelok cells for electrochemical measurements were assembled in air at room temperature. The cells were built with CaVOnH positive electrode, AC counter electrode, AgCl/Ag reference electrode (3 M NaCl), 0.8 m Mg(TFSI)₂-85%PEG-15%H₂O or 0.8 m Mg(TFSI)₂-65%PEG-20%DMSO-15%H₂O as an electrolyte (700 μL), and a piece of glass microfiber (Whatman) as the separator. AC was used as the counter electrode because of its high specific surface area, which can provide sufficient charge storage via electrical double-layer capacitance to guarantee full charge balance during Mg intercalation[16,20]. The mass of AC was intentionally in excess with a large N/P ratio of about 9–12. Note that the specific capacities were calculated according to the weight of the active cathode material. Galvanostatic cycling with potential limitation (GCPL) and cyclic voltammetry (CV) measurements were performed between -1.0 and 1.1 V (vs AgCl/Ag, 3 M NaCl) on a VMP3 potentiostat (BioLogic) at 25 °C. GCPL was performed at different current densities ranging from 50 to 1000 mA g⁻¹ to determine the rate capability of the electrodes. All potentials have been converted to Mg²⁺/Mg reference for convenience based on the voltage difference of 2.58 V between AgCl/Ag and Mg²⁺/Mg.

3.1.5. In operando synchrotron diffraction and in operando X-ray absorption spectroscopy (XAS)

In operando synchrotron diffraction was performed at PETRA-III beamline P02.1 at DESY in Hamburg, Germany[49] (λ=0.20733 Å, 60 keV). The electrochemical cell consists of 2025-type coin cell with Kapton windows of 5 mm diameter for beam entrance. The cell was prepared using coated CaVOnH positive electrode on carbon paper, AC counter electrode, Whatman separator, and 0.8 m Mg(TFSI)₂-85%PEG-15%H₂O. In operando synchrotron diffraction was conducted with radiation λ= 0.20733 Å wavelength (60 keV) with an effective exposure time of 40 s and current density of 25 mA g⁻¹. The diffraction data analysis was carried out by the Rietveld method using the Fullprof software package[50]. In operando XAS measurements were performed at synchrotron beamline P65 at PETRA III (DESY, Hamburg)[51]. XAS was recorded during the first charge/discharge process at the current of 25 mA g⁻¹ in the same coin-cell configuration. The cell was prepared using pressed CaVOnH positive electrode on stainless steel mesh within a 5 mm hole in the center, AC counter electrode, Whatman separator, and 0.8 m Mg(TFSI)₂-65%PEG-20%AN-15%H₂O (AN, Acetonitrile). XAS spectra at the V K-edge were recorded in quick-XAS (6 min/spectrum) mode in fluorescence geometry using PIPS (passivated implanted planar silicon) diode detector. The monochromator was calibrated at 5464.75 eV using a vanadium foil and V K-edge spectra for CaVOnH were measured. V₂O₃, VO₂, and V₂O₅ were used as standard materials. All data were collected at room temperature with a double crystal

monochromator of Si(111) crystal, and all XAS spectra were processed using the DEMETER software package[52].

3.1.6. Sample preparation for ex situ characterizations

The cells of three materials were disassembled and washed with acetonitrile in an Ar-filled glovebox for the first discharged states (2.0 V and 1.58 V) and charged states (2.7 V and 3.68 V). *Ex situ* XAS measurements were carried out at PETRA-III beamline P65 at DESY in Hamburg[51]. XAS spectra were recorded in quick-XAS (6 min/spectrum) mode in fluorescence geometry using the PIPS diode. The V K-edge of CaVOH at different states was measured and the energy was calibrated using the absorption edge of V foil, as it is commonly employed in XAS experiments.

3.2. Molecular dynamics simulations

All atomistic molecular dynamics (MD) simulations were performed with the GROMACS 4.6.7 package[53]. The GROMOS force field[54] was used for all components. The MD simulations were carried out using cubic cells with a linear dimension of 2.35 nm for 0.8 m Mg(TFSI)₂-65% PEG-20%DMSO-15%H₂O (containing 10 Mg(TFSI)₂, 100 H₂O, 20 PEG, and 30 DMSO) using the software package PACKMOL[55]. In all simulations, the temperature was kept constant at $T = 300$ K by an improved velocity-rescaling thermostat[56], using a coupling time constant of 0.1 ps. The pressure was kept constant at $p = 1$ bar by a semi-isotropic Parrinello-Rahman barostat[57] with coupling time constant of 2 ps and compressibility 4.5×10^{-5} bar. Electrostatic interactions were treated through the Particle Mesh Ewald method[58] with a real-space cut-off of 1.0 nm and a grid spacing of 0.16 nm with fourth-order interpolation scheme. Lennard-Jones interactions were truncated at 1.0 nm and shifted to zero. A Leapfrog algorithm with an elementary time step of 2 fs was used for numerical integration. All bonds were constrained by the LINCS algorithm[59]. Prior to production runs, energy minimization was first performed using a conjugate-gradient method, followed by equilibration of the system for 10 ns under constant volume constant temperature conditions, and a subsequent equilibration run of 10 ns under constant temperature and constant pressure conditions. These final production runs at constant temperature and pressure had a length of more than 150 ns each.

Author contributions

Q.F. conceived the idea and discussed with X.W., X.L., Z.D., S.I., A.S., Z.M., M.D., Z.W., W.H., K.C., B.S., M.K., H.E., Y.W., and S.D.; Q.F. performed material synthesis, electrolyte/sample preparation, characterizations, electrochemical measurements, and analyzed the data. Z.D. carried out the electron diffraction measurements and analyzed the data with K.C.. Z.W. carried out viscosity measurements and analyzed viscosity data. Z.M. performed TGA-MS measurement and analyzed the data. S.I. conducted NMR and analyzed the data. B.S. carried out magnetic measurements and analyzed the data. X.L. performed XPS and Raman measurements and analyzed the XPS data and Q.F. analyzed the Raman data. A.S., M.D., and Q.F. carried out *in operando* XAS and analyzed the data. M.K., W.H., and Q.F. carried out *in operando* synchrotron diffraction and analyzed the data. X.W. carried out DFT and MD calculations and analyzed the data with Y.W.. Q.F. wrote the preliminary draft with input from X.W. and Y.W.; Q.F., M.K., H.E., S.D., and Y.W. discussed the results and revised the manuscript. All authors contributed to interpreting the findings, reviewing, and commenting on the manuscript.

CRediT authorship contribution statement

Qiang Fu: Conceptualization, Investigation, Methodology, Supervision, Writing – original draft, Writing – review & editing. **Xiaoyu Wu:** Investigation, Writing – review & editing. **Xianlin Luo:** Investigation,

Writing – review & editing. **Ziming Ding:** Investigation, Writing – review & editing. **Sylvio Indris:** Investigation, Writing – review & editing. **Angelina Sarapulova:** Investigation, Writing – review & editing. **Zhen Meng:** Investigation, Writing – review & editing. **Morgane Desmau:** Investigation, Writing – review & editing. **Zhengqi Wang:** Investigation, Writing – review & editing. **Weibo Hua:** Investigation, Writing – review & editing. **Christian Kübel:** Investigation, Writing – review & editing. **Björn Schwarz:** Investigation, Methodology, Writing – review & editing. **Michael Knapp:** Investigation, Writing – review & editing. **Helmut Ehrenberg:** Funding acquisition, Resources, Supervision, Writing – review & editing. **Yingjin Wei:** Conceptualization, Funding acquisition, Resources, Supervision, Writing – review & editing. **Sonia Dsoke:** Methodology, Supervision, Writing – review & editing.

Declaration of competing interest

The authors declare that they have no known competing financial interests or personal relationships that could have appeared to influence the work reported in this paper.

Data availability

Data will be made available on request.

Acknowledgments

This work contributes to the research performed at CELEST (Center for Electrochemical Energy Storage Ulm-Karlsruhe) and was partially funded by the Deutsche Forschungsgemeinschaft (DFG, German Research Foundation) under Germany's Excellence Strategy – EXC 2154 – Project ID 390874152 (POLiS Cluster of Excellence). This work was also supported by National Natural Science Foundation of China (No. 51972140). We acknowledge DESY (Hamburg, Germany), a member of the Helmholtz Association HGF, for the provision of experimental facilities. Parts of this research were carried out at beamtime P02.1 and P65 and we would like to thank Volodymyr Baran and Edmund Welter for their technical supports. Beamtime was allocated for proposals I-20210736 at P02.1 and I-20200899 at P65. We also want to acknowledge the support and collaboration from Andreas Hofmann and Thomas Hanemann within POLiS. We thank Holger Geßwein and Bettina Hunzinger for their contribution to spatially resolved XRD and SEM measurements, respectively. We greatly appreciate Liuda Mereacre for her support in TGA and Raman measurements. Thomas Bergfeldt (IAM-AWP) is gratefully acknowledged for ICP-OES measurements. We acknowledge the Karlsruhe Nano Micro Facility at Karlsruhe Institute of Technology for providing TEM access.

Supplementary materials

Supplementary material associated with this article can be found, in the online version, at [doi:10.1016/j.ensm.2024.103212](https://doi.org/10.1016/j.ensm.2024.103212).

The original data are available at KITOpen through the DOI: doi.org/10.35097/1858.

References

- [1] M. Mao, T. Gao, S. Hou, C. Wang, A critical review of cathodes for rechargeable Mg batteries, *Chem. Soc. Rev.* 47 (2018) 8804–8841.
- [2] H.D. Yoo, I. Shterenberg, Y. Gofer, G. Gershinsky, N. Pour, D. Aurbach, Mg rechargeable batteries: an on-going challenge, *Energy Environ. Sci.* 6 (2013) 2265–2279.
- [3] D. Aurbach, Z. Lu, A. Schechter, Y. Gofer, H. Gizbar, R. Turgeman, Y. Cohen, M. Moshkovich, E. Levi, Prototype systems for rechargeable magnesium batteries, *Nature* 407 (2000) 724–727.
- [4] E. Levi, M.D. Levi, O. Chasid, D. Aurbach, A review on the problems of the solid state ions diffusion in cathodes for rechargeable Mg batteries, *J. Electroceram.* 22 (2009) 13–19.

- [5] F. Liu, T. Wang, X. Liu, L.-Z. Fan, Challenges and Recent Progress on Key Materials for Rechargeable Magnesium Batteries, *Adv. Energy Mater.* 11 (2020) 2000787.
- [6] Z. Ma, D.R. MacFarlane, M. Kar, Mg Cathode Materials and Electrolytes for Rechargeable Mg Batteries: a Review, *Batter. Supercaps* 2 (2019) 115–127.
- [7] R. Deivanayagam, B.J. Ingram, R. Shabbazian-Yassar, Progress in development of electrolytes for magnesium batteries, *Energy Storage Mater.* 21 (2019) 136–153.
- [8] R. Mohtadi, O. Tutasaus, CHAPTER 2 non-aqueous electrolytes for Mg batteries, magnesium batteries: research and applications, *Roy. Soc. Chem.* (2020) 17–59.
- [9] F. Wang, X. Fan, T. Gao, W. Sun, Z. Ma, C. Yang, F. Han, K. Xu, C. Wang, High-Voltage Aqueous Magnesium Ion Batteries, *ACS Cent. Sci.* 3 (2017) 1121–1128.
- [10] L. Chen, J.L. Bao, X. Dong, D.G. Truhlar, Y. Wang, C. Wang, Y. Xia, Aqueous Mg-ion battery based on polyimide anode and prussian blue cathode, *ACS Energy Lett.* 2 (2017) 1115–1121.
- [11] H. Zhang, K. Ye, X. Huang, X. Wang, K. Cheng, X. Xiao, G. Wang, D. Cao, Preparation of $\text{Mg}_{1.1}\text{Mn}_6\text{O}_{12} \cdot 4.5\text{H}_2\text{O}$ with nanobelt structure and its application in aqueous magnesium-ion battery, *J. Power. Source.* 338 (2017) 136–144.
- [12] G. Liu, Q. Chi, Y. Zhang, Q. Chen, C. Zhang, K. Zhu, D. Cao, Superior high rate capability of $\text{MgMn}_2\text{O}_4/\text{rGO}$ nanocomposites as cathode materials for aqueous rechargeable magnesium-ion batteries, *Chem. Commun.* 54 (2018) 9474–9477.
- [13] Y. Zhang, G. Liu, C. Zhang, Q. Chi, T. Zhang, Y. Feng, K. Zhu, Y. Zhang, Q. Chen, D. Cao, Low-cost $\text{MgFe}_x\text{Mn}_{2-x}\text{O}_4$ cathode materials for high-performance aqueous rechargeable magnesium-ion batteries, *Chem. Eng. J.* 392 (2018) 123652.
- [14] D. Chao, W. Zhou, F. Xie, C. Ye, H. Li, M. Jaroniec, S.-Z. Qiao, Roadmap for advanced aqueous batteries: from design of materials to applications, *Sci. Adv.* 6 (2020) eaba4098.
- [15] J. Yao, Y. Li, R.C. Massé, E. Uchaker, G. Cao, Revitalized interest in vanadium pentoxide as cathode material for lithium-ion batteries and beyond, *Energy Storage Mater.* 11 (2018) 205–259.
- [16] J.L. Andrews, A. Mukherjee, H.D. Yoo, A. Parija, P.M. Marley, S. Fakra, D. Prendergast, J. Cabana, R.F. Klie, S. Banerjee, Reversible Mg-ion insertion in a metastable one-dimensional polymorph of V_2O_5 , *Chem* 4 (2018) 564–585.
- [17] Y.-H. Zhu, Q. Zhang, X. Yang, E.-Y. Zhao, T. Sun, X.-B. Zhang, S. Wang, X.-Q. Yu, J.-M. Yan, Q. Jiang, Reconstructed orthorhombic V_2O_5 polyhedra for fast ion diffusion in K-ion batteries, *Chem* 5 (2019) 168–179.
- [18] Q. Fu, A. Sarapulova, L. Zhu, G. Melinte, A. Missyul, E. Welter, X. Luo, M. Knapp, H. Ehrenberg, S. Dsoke, In operando study of orthorhombic V_2O_5 as positive electrode materials for K-ion batteries, *J. Energy Chem.* 62 (2021) 627–636.
- [19] X. Deng, Y. Xu, Q. An, F. Xiong, S. Tan, L. Wu, L. Mai, Manganese ion pre-intercalated hydrated vanadium oxide as a high-performance cathode for magnesium ion batteries, *J. Mater. Chem. A* 7 (2019) 10644–10650.
- [20] Y. Xu, X. Deng, Q. Li, G. Zhang, F. Xiong, S. Tan, Q. Wei, J. Lu, J. Li, Q. An, L. Mai, Vanadium oxide pillared by interlayer Mg^{2+} ions and water as ultralong-life cathodes for magnesium-ion batteries, *Chem* 5 (2019) 1194–1209.
- [21] Q. Fu, X. Wu, X. Luo, S. Indris, A. Sarapulova, M. Bauer, Z. Wang, M. Knapp, H. Ehrenberg, Y. Wei, S. Dsoke, High-voltage aqueous Mg-ion batteries enabled by solvation structure reorganization, *Adv. Funct. Mater.* 32 (2022) 2110674.
- [22] H. Wang, Y. Deng, J. Qiu, J. Wu, K. Zhang, J. Shao, L. Yan, In situ formation of “dimethyl sulfoxide/water-in-salt”-based chitosan hydrogel electrolyte for advanced all-solid-state supercapacitors, *ChemSusChem* 14 (2021) 632–641.
- [23] Y. Oka, T. Yao, N. Yamamoto, Crystal structures of hydrated vanadium oxides with δ -type V_2O_5 layers: $\delta\text{-M}_{0.25}\text{V}_2\text{O}_5 \cdot \text{H}_2\text{O}$, $\text{M}=\text{Ca}$, Ni , *J. Solid. State Chem.* 132 (1997) 323–329.
- [24] E. Potiron, A. Le Gal La Salle, A. Verbaere, Y. Piffard, D. Guyomard, Electrochemically synthesized vanadium oxides as lithium insertion hosts, *Electrochim. Acta* 45 (1999) 197–214.
- [25] E. Potiron, A. Le Gal La Salle, A. Verbaere, Y. Piffard, D. Guyomard, M. Tournoux, Electrochemical synthesis, characterization and lithium intercalation properties of $\text{e-M}_x\text{V}_2\text{O}_5 \cdot y\text{-nH}_2\text{O}$ ($\text{M}=\text{NiII}$, CuII or MnIV), *J. Phys. Chem. Solid.* 62 (2001) 1447–1455.
- [26] H. Wang, X. Bi, Y. Bai, C. Wu, S. Gu, S. Chen, F. Wu, K. Amine, J. Lu, Open-structured $\text{V}_2\text{O}_5 \cdot n\text{H}_2\text{O}$ nanoflakes as highly reversible cathode material for monovalent and multivalent intercalation batteries, *Adv. Energy Mater.* 7 (2017) 1602720.
- [27] D. Kundu, B.D. Adams, V. Duffort, S.H. Vajargah, L.F. Nazar, A high-capacity and long-life aqueous rechargeable zinc battery using a metal oxide intercalation cathode, *Nat. Energy* 1 (2016) 16119.
- [28] H. Zhao, Q. Fu, D. Yang, A. Sarapulova, Q. Pang, Y. Meng, L. Wei, H. Ehrenberg, Y. Wei, C. Wang, G. Chen, In operando synchrotron studies of NH_4^+ pre-intercalated $\text{V}_2\text{O}_5 \cdot n\text{H}_2\text{O}$ nanobelts as the cathode material for aqueous rechargeable zinc batteries, *ACS Nano* 14 (2020) 11809–11820.
- [29] E.A. Esparcia, M.S. Chae, J.D. Ocon, S.-T. Hong, Ammonium vanadium bronze ($\text{NH}_4\text{V}_4\text{O}_{10}$) as a high-capacity cathode material for nonaqueous magnesium-ion batteries, *Chem. Mater.* 30 (2018) 3690–3696.
- [30] G. Silversmit, D. Depla, H. Poelman, G.B. Marin, R. De Gryse, Determination of the V2p XPS binding energies for different vanadium oxidation states (V^{5+} to V^{0+}), *J. Electron. Spectros. Relat. Phenomena* 135 (2004) 167–175.
- [31] G.A. Muller, J.B. Cook, H.-S. Kim, S.H. Tolbert, B. Dunn, High performance pseudocapacitor based on 2D layered metal chalcogenide nanocrystals, *Nano Lett.* 15 (2015) 1911–1917.
- [32] C. Schreiner, S. Zugmann, R. Hartl, H.J. Gores, Fractional walden rule for ionic liquids: examples from recent measurements and a critique of the So-called ideal KCl line for the Walden Plot, *J. Chem. Eng. Data* 55 (2010) 1784–1788.
- [33] T. Tanaka, H. Yamashita, R. Tsuchitani, T. Funabiki, S. Yoshida, X-ray absorption (EXAFS/XANES) study of supported vanadium oxide catalysts. Structure of surface vanadium oxide species on silica and [gamma]-alumina at a low level of vanadium loading, *J. Chem. Soc. Faraday Transact. 1: Phys. Chem. Condens. Phase.* 84 (1988) 2987–2999.
- [34] J. Wong, F.W. Lytle, R.P. Messmer, D.H. Maylotte, K-edge absorption spectra of selected vanadium compounds, *Phys. Rev. B* 30 (1984) 5596–5610.
- [35] S. Passerini, W.H. Smyrl, M. Berrettoni, R. Tossici, M. Rosolen, R. Marassi, F. Decker, XAS and electrochemical characterization of lithium intercalated V_2O_5 xerogels, *Solid. State Ion.* 90 (1996) 5–14.
- [36] H.D. Yoo, Y. Liang, H. Dong, J. Lin, H. Wang, Y. Liu, L. Ma, T. Wu, Y. Li, Q. Ru, Y. Jing, Q. An, W. Zhou, J. Guo, J. Lu, S.T. Pantelides, X. Qian, Y. Yao, Fast kinetics of magnesium monochloride cations in interlayer-expanded titanium disulfide for magnesium rechargeable batteries, *Nat. Commun.* 8 (2017) 339.
- [37] X. Liu, D. Wang, G. Liu, V. Srinivasan, Z. Liu, Z. Hussain, W. Yang, Distinct charge dynamics in battery electrodes revealed by in situ operando soft X-ray spectroscopy, *Nat. Commun.* 4 (2013) 2568.
- [38] S. Stizza, G. Mancini, M. Benfatto, C.R. Natoli, J. Garcia, A. Bianconi, Structure of oriented V_2O_5 gel studied by polarized X-ray-absorption spectroscopy at the vanadium K edge, *Phys. Rev. B: Condens. Matter* 40 (1989) 12229–12236.
- [39] A.N. Mansour, P.H. Smith, M. Balasubramanian, J. McBreen, *In situ* X-ray absorption study of cycled ambigal $\text{V}_2\text{O}_5 \cdot n\text{H}_2\text{O}$ ($n \approx 0.5$) composite cathodes, *J. Electrochem. Soc.* 152 (2005) A1312.
- [40] M. Giorgetti, *In situ* X-ray absorption spectroscopy characterization of V_2O_5 xerogel cathodes upon lithium intercalation, *J. Electrochem. Soc.* 146 (1999) 2387.
- [41] R. Baddour-Hadjean, J.P. Pereira-Ramos, C. Navone, M. Smirnov, Raman microspectrometry study of electrochemical lithium intercalation into sputtered crystalline V_2O_5 thin films, *Chem. Mater.* 20 (2008) 1916–1923.
- [42] M. Huang, X. Wang, J. Wang, J. Meng, X. Liu, Q. He, L. Geng, Q. An, J. Yang, L. Mai, Proton/ Mg^{2+} Co-Insertion Chemistry in Aqueous Mg-Ion Batteries: from the Interface to the Inner, *Angewand. Chem. Int. Ed.* 62 (2023) e202308961.
- [43] T. Gao, S. Hou, K. Huynh, F. Wang, N. Eidson, X.L. Fan, F.D. Han, C. Luo, M.L. Mao, X.G. Li, C.S. Wang, Existence of solid electrolyte interphase in Mg batteries: Mg/S chemistry as an example, *ACS. Appl. Mater. Interface.* 10 (2018) 14767–14776.
- [44] B. Li, R. Masse, C.F. Liu, Y. Hu, W.S. Li, G.Q. Zhang, G.Z. Cao, Kinetic surface control for improved magnesium-electrolyte interfaces for magnesium ion batteries, *Energy Storage Mater.* 22 (2019) 96–104.
- [45] <https://www.jems-swiss.ch/Home/jemsWebSite/jems.html>.
- [46] K.L. Parry, A.G. Shard, R.D. Short, R.G. White, J.D. Whittle, A. Wright, ARXPS characterisation of plasma polymerised surface chemical gradients, *Surface Interface Anal.* 38 (2006) 1497–1504.
- [47] J.H. Scofield, Hartree-Slater subshell photoionization cross-sections at 1254 and 1487 eV, *J. Electron. Spectros. Relat. Phenomena* 8 (1976) 129–137.
- [48] S. Tanuma, C.J. Powell, D.R. Penn, Calculations of electron inelastic mean free paths. IX. Data for 41 elemental solids over the 50 eV to 30 keV range, *Surface Interface Anal.* 43 (2011) 689–713.
- [49] M. Herklotz, F. Scheiba, M. Hinterstein, K. Nikolowski, M. Knapp, A.-C. Dippel, L. Giebeler, J. Eckert, H. Ehrenberg, Advances in in situ powder diffraction of battery materials: a case study of the new beamline P02.1 at DESY, Hamburg, *J. Appl. Crystallogr.* 46 (2013) 1117–1127.
- [50] J. Rodríguez-Carvajal, Recent developments of the program FULLPROF, in commission on powder diffraction (IUCr), *Newsletter* 26 (2001) 12–19.
- [51] E. Welter, R. Chernikov, M. Herrmann, R. Nemausat, A beamline for bulk sample x-ray absorption spectroscopy at the high brilliance storage ring PETRA III, *AIP. Conf. Proc.* 2054 (2019) 040002.
- [52] B. Ravel, M. Newville, ARTEMIS ATHENA, HEPHAESTUS: data analysis for X-ray absorption spectroscopy using IFFEFIT, *J. Synchrotron. Radiat.* 12 (2005) 537–541.
- [53] B. Hess, C. Kutzner, D. van der Spoel, E. Lindahl, GROMACS 4: algorithms for highly efficient, load-balanced, and scalable molecular simulation, *J. Chem. Theory. Comput.* 4 (2008) 435–447.
- [54] C. Oostenbrink, A. Villa, A.E. Mark, W.F. Van Gunsteren, A biomolecular force field based on the free enthalpy of hydration and solvation: the GROMOS force-field parameter sets 53A5 and 53A6, *J. Comput. Chem.* 25 (2004) 1656–1676.
- [55] L. Martínez, R. Andrade, E.G. Birgin, J.M. Martínez, PACKMOL: a package for building initial configurations for molecular dynamics simulations, *J. Comput. Chem.* 30 (2009) 2157–2164.
- [56] G. Bussi, D. Donadio, M. Parrinello, Canonical sampling through velocity rescaling, *J. Chem. Phys.* 126 (2007) 014101.
- [57] M. Parrinello, A. Rahman, Polymorphic transitions in single crystals: a new molecular dynamics method, *J. Appl. Phys.* 52 (1981) 7182–7190.
- [58] T. Darden, D. York, L. Pedersen, Particle mesh Ewald: an $N\log(N)$ method for Ewald sums in large systems, *J. Chem. Phys.* 98 (1993) 10089–10092.
- [59] B. Hess, H. Bekker, H.J.C. Berendsen, J.G.E.M. Fraaije, LINC: a linear constraint solver for molecular simulations, *J. Comput. Chem.* 18 (1997) 1463–1472.